Contrasting stable water isotope signals from convective and large-scale precipitation phases of a heavy precipitation event in Southern Italy during HyMeX IOP 13: a modelling perspective

Keun-Ok Lee[1], Franziska Aemisegger[2], Stephan Pfahl[2,3], Cyrille Flamant[4], Jean-Lionel Lacour[5], and Jean-Pierre Chaboureau[1]

[1]Laboratoire d'Aérologie, Université de Toulouse, CNRS, UPS, Toulouse, France
[2]Institute for Atmospheric and Climate Science, ETH Zurich, 8092 Zurich, Switzerland
[3]Institute of Meteorology, Freie Universität Berlin, Berlin, Germany
[4]LATMOS/IPSL, CNRS, Sorbonne Université and Université Paris-Saclay, Paris, France
[5]Institute of Earth Sciences, University of Iceland, Reykjavik, Iceland

ABSTRACT

The dynamical context and moisture transport pathways embedded in large scale flow and associated with a heavy precipitation event (HPE) in Southern Italy (SI) are investigated with the help of stable water isotopes (SWIs) based on a purely numerical framework. The event occurred during the intensive observation period (IOP) 13 of the field campaign of the Hydrological Cycle in the Mediterranean Experiment (HyMeX) on 15 and 16 October 2012 and SI experienced intense rainfall of 62.4 mm over 27 h with two precipitation phases during this event. The first one (P1) was induced by convective precipitation linked to a frontal feature, while the second one (P2) was mainly associated with precipitation induced by large-scale uplift. The moisture transport and processes responsible for the HPE are analysed using a simulation with the isotope-enabled regional numerical model $\mathrm{COSMO_{iso}}$. Backward trajectory analyses based on this simulation show that the air parcels arriving in SI during P1 originate from the North Atlantic, and descend within an upper-level trough over the north-western Mediterranean. The descending air parcels reach elevations below 1 km over the sea and bring dry and isotopically depleted air (median $\delta^{18}O \leq -25$ ‰, water vapour mixing ratio $q \leq 2$ g kg^{-1}) close to the surface, which induces strong surface evaporation. These air parcels are rapidly enriched in SWI ($\delta^{18}O \geq -14$ ‰) and moistened ($q \geq 8$ g kg^{-1}) over the Tyrrhenian Sea by taking up moisture from surface evaporation and potentially from evaporation of frontal precipitation. Thereafter, the SWI-enriched low-level air masses arriving upstream of SI are convectively pumped to higher altitudes, and the SWI-depleted moisture from higher levels is transported towards the surface within the downdrafts ahead of the cold front over SI, producing a large amount of precipitation of convective nature in SI. Most of the moist processes (i.e. evaporation, convective mixing) related to the HPE take place during the 18 hours preceding the occurrence of P1 over SI. Four hours later, during the second precipitation phase P2, the air parcels arriving over SI mainly originate from North Africa. The strong cyclonic flow around the eastward moving upper-level trough induces the advection of a moist and SWI-enriched African plume towards SI, and leads to large-scale uplift of the warm African air mass along the cold front. This brings moist and SWI-enriched air masses (median $\delta^{18}O \geq -16$ ‰, median $q \geq 6$ g kg^{-1}) to higher altitudes and leads to gradual rain out of the air parcels over Italy. Large-scale ascent in the warm sector ahead of the cold front takes place during the 72 hours preceding P2 in SI. This work demonstrates how stable water isotopes can yield additional insights into the variety of thermodynamic mechanisms occurring at the meso- and synoptic scales during the formation of a HPE.

1. Introduction

The Mediterranean basin is frequently affected by deep convection resulting in heavy precipitation and potentially leading to devastating flash floods. Deep convection generally results from complex multi-scale interactions between large-scale, mesoscale, and microphysical processes. In the north-western Mediterranean, the large-scale patterns associated with heavy precipitation events (HPEs) have been shown to be connected to upper-level troughs, responsible for generating low-level northward flow of marine air masses characterized by high values of equivalent potential temperature and precipitable water (Lin et al., 2001; Martius et al., 2006; Nuissier et al., 2008, 2011; Ricard et al., 2012; Barthlott and Davolio, 2015). In this favourable large-scale situation, mesoscale deep convection can occur and often produces high-impact events, along with rainfall amounts larger than 100 mm in less than 6 hours. The origin of the moisture content feeding the deep convective systems is an important question that has been addressed using different techniques and tools, such as trajectory and numerical tracer analyses (*e.g.* Turato et al. 2004; Winschall et al., 2012; Duffourg and Ducrocq, 2013; Winschall et al., 2014; Röhner et al., 2016; Duffourg et al., 2018; Lee et al., 2018). These studies found substantial contributions of subtropical and tropical moisture coming either from Africa (latitude ≥ 20°N) or from the extratropical remnants of Atlantic tropical cyclones. More recent studies (*e.g.* Lee et al.

2016 and 2017) pointed out the intrusion of large moisture, e.g. one quarter of total integrated water vapour, from North Africa in the mid-troposphere (3-5 km above sea level, ASL) feeding the deep convective systems together with the local water vapour sources over the Mediterranean in the lower troposphere (below 2 km ASL). Moreover, the importance of intensified evaporation over the Mediterranean Sea surface for HPE has been studied (Duffourg and Ducrocq, 2013; Winschall et al., 2014). The vertical distribution of moisture in the atmosphere is shaped by source, transport, and sink processes, e.g. evaporation and condensation, horizontal and vertical advection, as well as turbulent and convective mixing.

To improve our understanding of the water vapour transport upstream of HPEs and the moisture cycling during such events, humidity observations based on measurements of the most abundant stable water isotopes (SWI) $H_2{}^{16}O$ alone can be limited. In this context, the SWI observation of other, less abundant SWIs, i.e. $H_2{}^{18}O$ and $HD^{16}O$ can provide relevant additional constrains (Noone et al., 2012; Pfahl et al., 2012; Aemisegger et al. 2015; Galewsky et al., 2016; Sodemann et al., 2017). Heavy and light isotopes of the water molecule are partitioned in a very specific way during phase transitions, leading to an enrichment of the heavier molecules compared to the lighter ones in the phase with the stronger bonds (liquid or ice) and a depletion in vapour. Therefore, they can provide a record of evaporation and condensation cycles during the transport of air parcels. Since the strength of fractionation depends on the meteorological conditions (temperature and the level of saturation), SWI are a powerful indicator of phase change conditions in the atmosphere that occur during the transport of air parcels on a broad range of scales, reflecting evaporation, condensation, and air mass mixing processes (e.g., Sodemann et al., 2017). For instance, low δ^2H (typical range between –160 and –180 ‰) or $\delta^{18}O$ (i.e. range between –20 and –30 ‰) values in atmospheric water vapour at surface indicate low air mass temperatures and strong rainout of air parcels (e.g. Jacob and Sonntag, 1991; Yoshimura et al., 2010), whereas high δ^2H (typical range between –120 and –100 ‰) or $\delta^{18}O$ (range between –18 and –14 ‰) indicate high air mass temperatures and recent admixture of fresh ocean evaporate. The δ notation describes the concentrations of the heavy isotopes relative to the isotope ratio of the Vienna Standard Mean Ocean Water– RVSMOW, by for instance, $\delta^{18}O = (Rs/RVSMOW - 1) \times 1000$, where $Rs = [H_2{}^{18}O]/[H_2{}^{16}O]$ is the isotope ratio of a water sample.

In the past, some of the most prominent applications of SWIs have been in a paleoclimate context to infer past temperatures and moisture sources from natural archives, for groundwater studies, and in studies investigating the water vapour budget in the stratosphere (Sherwood and Dessler, 2000; Vimeux et al., 2001;

Dessler and Sherwood, 2003; Jouzel et al., 2005). The process-based insight provided by the isotope composition of atmospheric water have more recently been extended to synoptic and sub-diurnal timescales and to the lower troposphere, where most atmospheric water vapour resides. Thanks to a tremendous expansion in the number of datasets of water vapour isotopic composition and a substantially improved set of theories and models for interpreting them, the related studies have been expanded during the past several years (*e.g.* Pfahl et al. 2008; Steen-Larsen et al. 2014; Bonne et al. 2014; Aemisegger et al. 2015; Dütsch et al., 2017; Lacour et al., 2017; Christner et al., 2018).

Recent studies have shown the unique information about meteorological processes registered in SWI data. For instance, using ground-based SWI measurements and numerical simulations, Pfahl et al. (2012) and Aemisegger et al. (2015) investigated the mixing processes of different air masses, as well as isotope fractionation and equilibration in relationship with precipitation evaporation, during the passage of cold fronts. Aemisegger and Papritz (2018) and Aemisegger and Sjolte (2018) showed that the important moisture uptake by cold and dry airstreams during events of strong large-scale ocean evaporation carries a distinct SWI-signature in water vapour. Recent studies (Schneider et al. 2016; Lacour et al. 2017) analysed the influence of the Saharan heat low on the isotopic budget of the free troposphere offshore of West Africa on various temporal and spatial scales, highlighting the importance of the Saharan heat low dynamics on the moistening and the SWI enrichment of air parcels in the free troposphere over the North Atlantic. In addition, Risi et al. (2008) used stable isotopic signals to better understand convective precipitation processes. These previous studies evidenced the usefulness of water vapour isotope data to better understand meteorological processes and moisture transport. Nevertheless, there are still very few studies (Risi et al., 2008 and 2010; Tremoy et al., 2014) focusing on the application of water vapour isotopes to investigate moist processes associated with HPEs at the mesoscale, particularly in the extratropics.

SWI measurements are mainly obtained from space-borne retrievals (e.g. Schneider et al., 2016; Lacour et al., 2017) and ground-based in-situ laser spectroscopy (e.g. Aemisegger et al., 2012). The space-borne measurements provide continuous datasets in space at the global scale with coarse vertical resolution and limited precision. On the other hand, ground-based measurements with high temporal resolution are only available from a few locations and from dedicated field campaigns. In particular, the data availability for the Mediterranean region is very limited. A notable exception is the airborne dataset acquired around Corsica (Sodemann et al., 2017) during the first Special Observing Period of the Hydrological cycle in the

Mediterranean Experiment (HyMeX SOP-1, Ducrocq et al., 2014). However, it does not include SWI observations for the days under scrutiny in this paper. Due to these limitations we use a model to demonstrate the usefulness of SWI data for understanding moist processes associated with a Mediterranean HPE.

Our study focuses on the transport of moisture associated with a HPE that occurred over southern Italy (SI) on 15−16 October 2012 and produced precipitation over land exceeding 60 mm in 27 h (Fig. 1a). The HPE consists of two precipitation peaks, the first peak in the late afternoon of 15 October and the second peak around midnight on that day. The target HPE occurred during the Intensive Observation Period 13 (IOP 13) of the HyMeX SOP-1. Using a combination of ground-based, airborne and space-borne observations and numerical simulations of this HPE, Lee et al. (2016) investigated the detailed dynamic and thermodynamic environments of the two precipitation phases of the HPE. During Phase 1 (P1), rainfall was connected to convection triggered by local low-level convergence ahead of a cold front and was favoured by moist conditions in the low levels over the Tyrrhenian Sea. Heavy precipitation during Phase 2 (P2) was initiated over Algeria and was favoured by the southerly flow ahead of the upper-level trough and large low-level moisture content and high sea surface temperature in the Strait of Sicily. The penetration of the mistral over the Mediterranean and SI at the end of 15 October terminated the convective activity. Thanks to the unprecedented data acquired offshore and inland during IOP 13, the detailed moisture structure upstream of the HPE was investigated by Lee et al. (2016). However, the origin and transport pathways of moisture have not been studied to date.

Here we investigate these moisture transport processes using trajectory calculations and SWI data obtained from a numerical simulation with 7-km horizontal resolution. A detailed description of the data and methodology is presented in section 2. Section 3 provides an overview of the meteorological conditions during the two precipitation peaks related to the HPE during IOP 13. Section 4 discusses the isotope signals and relates them to the moisture transport history. A summary and a discussion of the findings of the present study are given in section 5.

2. Data and method

2.1. COSMOiso model configuration and simulation

The COSMO model (Steppeler et al., 2003) is a non-hydrostatic, limited-area numerical weather and climate prediction model and is operationally used by several European weather services. The isotope implementation (COSMOiso; Pfahl et al., 2012) is similar to other Eulerian isotope models (e.g. Joussaume et al., 1984; Sturm et al., 2005; Blossey et al., 2010). COSMOiso has already shown its capability to simulate the variations of stable water isotopes at the event-timescale (Pfahl et al., 2012; Aemisegger et al. 2015) as well as in a climatological sense (Christner et al. 2018; Dütsch et al. 2018). It includes two additional parallel water cycles for each of the heavy isotopes ($H_2{}^{18}O$, $HD^{16}O$), which are used purely diagnostically and do not affect other model components. All prognostic moisture fields, which are simulated by the model in terms of specific humidities, are duplicated twice, representing the specific humidities of $H_2{}^{18}O$ and $HD^{16}O$, respectively. From the prognostic specific humidity fields, the isotope ratios in usual δ-notation can be calculated. The heavy isotopes experience the same processes as the light isotope ($H_2{}^{16}O$), except during phase transition, when isotopic fractionation occurs. A one-moment microphysics scheme is used and deep convection is parameterised following Tiedtke (1989). In the microphysical scheme, transfer rates between the different water species during the formation of clouds and precipitation are specified. The heavy isotopes are affected by equilibrium fractionation during the formation of liquid clouds, and both non-equilibrium and equilibrium fractionation during the formation of ice clouds (using the predicted super-saturation) as well as the re-evaporation of rain drops. For the parameterisation of moist convection, all physical processes during simulated convective up- and downdrafts affect the heavy isotopes in a similar way as the standard light humidity, again taking into account equilibrium and non-equilibrium fractionation when appropriate. For a detailed description of the physics and isotope parameterisations, see Doms et al. (2011) and Pfahl et al. (2012), respectively.

Operational analysis data from the European Centre for Medium-Range Weather Forecasts (ECMWF) are used as boundary and initial conditions for the standard model variables. For the period in October 2012, these data are available every six hours with a spectral resolution of T1279 and 91 vertical levels and are interpolated to the COSMO grid. After the model initialisation, information from the analysis data is only used at the model boundaries, employing a relaxation scheme following Davies (1976). For the water isotopes, initial and boundary data are taken from a historical isotope global circulation model IsoGSM (which is based on the Scripps Experimental Climate Prediction Center's GSM that was used operationally for medium range forecasts at NCEP) simulation by Yoshimura et al. (2008), who performed these simulations using a nudging technique (see also Pfahl et al., 2012). The Scripps Experimental Climate Prediction Center's GSM was based on the medium range forecast model used at NCEP for making operational analysis and predictions.

In this study, a horizontal grid spacing of 0.0625° (in a rotated grid), corresponding to approximately 7 km, and 40 hybrid vertical levels are used. The model domain covers the northwestern Mediterranean, the east Atlantic, and the northern African regions (longitude ranging from –16.3 to 22.8°E and latitude ranging from 17.3 to 49.2°N). The simulation starts at 00 UTC on 12 October 2012, and runs for 5 days producing output fields every hour.

2.2. Trajectory calculation

Air parcel backward trajectories (Wernli and Davies, 1997; Sprenger and Wernli, 2015) are calculated using the three-dimensional wind fields from the COSMOiso simulation. In total 1440 trajectories per hourly time step are started from 60 grid points within a box over SI (bounded by 15.2°W, 16.6°W, 39.6°N, 41.3°N; Fig. 1) and 24 different vertical levels between 1000 and 400 hPa. The trajectories are computed five days back in time. Note that generally the COSMO trajectories move out of the regional model domain after 3 days. The air parcel position as well as the interpolated conditions (δ^{18}O, water vapour mixing ratio -q, surface evaporation) along the trajectories are written as an output every hour. In this study, two series of trajectories, starting at the times of the two precipitation peaks (20 UTC on 15 October 2012 and 00 UTC on 16 October 2012; lines in Fig. 2) over SI are discussed.

2.3. q−δ analysis

As variations in δ are tied to those in humidity, q, the q−δ space is often used for the interpretation of the information contained in δ. The theoretical framework for interpreting paired q−δ data is based on a set of simple models that account for mixing and a range of condensation conditions (Noone, 2012). The isotopic depletion of water vapour that undergoes condensation at equilibrium can be described by a Rayleigh distillation model as $\delta = (\alpha-1)\ \ln (q/q_0) + \delta_0$, in which q_0 and δ_0 are the humidity and the isotopic composition of the water vapour source, and α is the coefficient of fractionation. In this study, q_0 and δ_0 are set to 15 g kg^{-1} and −10 ‰, respectively. The mixing model is $\delta = q_0\ (\delta_0 - \delta_F)\ 1/q + \delta_F$, in which the subscript F denotes the flux into the volume of interest, here set to −12 ‰.

Mixing and distillation of water vapour from different sources can occur over a wide range of combinations and produce q−δ pairs in between these two boundary models. A Rayleigh model with a tropical water vapour source can generally be used to describe the lower limit of the domain of existence of q−δ pairs. The upper limit of this domain can be described by a mixing model between depleted and dry air from the upper troposphere and enriched and humid air from the tropical boundary layer. The large-scale distribution of water vapour isotope ratio is conveniently viewed as a balance between the depleting effects of condensation (such as in a Rayleigh processes), mixing of air masses with vapour of differing isotopic composition during large-scale transport and the enriching effects during supply from a boundary layer source (Noone 2008; Galewsky and Hurley 2010). Also note that raindrop re-evaporation can lead to q−δ pairs below the Rayleigh distillation model (Worden et al., 2007).

3. Overview of meteorological condition

3.1 One HPE with two precipitation phases over southern Italy

From 00 UTC on 15 October to 03 UTC on 16 October 2012, the SI area (box marked by 'SI' in Figure 1) was affected by a HPE, with two phases of precipitation. The large amount of maximum precipitation (in total 62.4 mm over 27 h) recorded by the rain gauge network (Fig.1a) is realistically reproduced by COSMOiso simulation (maximum precipitation of 59 mm, Fig. 1b) both in terms of amplitude and spatial distribution. The temporal evolution of the COSMOiso domain-averaged total precipitation within the SI area (bars in Figure 2) shows precipitation in excess of 10 mm within the SI between 19 UTC on 15 October and 01 UTC on 16 October. The period has two distinct precipitation phases: 1) a convective precipitation phase (**P1**) in the late afternoon (19−21 UTC) on 15 October (dashed line in Fig. 2), and 2) a large-scale precipitation phase (**P2**) just before midnight (22−00 UTC) on that day (solid line). The precipitation associated with P1 is delayed by 4 hours in the COSMOiso simulation compared to the precipitation recorded by the rain gauge network, which shows a peak at 16−18 UTC (grey line with dot in Fig. 2), while the precipitation during P2 phase is closely reproduced by the simulation with a reasonable timing (~1 hour early, with the measured peak occurring at 23−01 UTC). P1 is related to rain from the convection parameterization, and P2 is related to rain associated with large-scale vertical motion. The model, in contrast to the observation, does not produce two peaks in the total precipitation. These peaks can be seen by looking at the two precipitation types separately. In the following, 20 UTC on 15 October and 00 UTC on 16 October are considered as times representative of P1 and P2, respectively, while 16 UTC on 15 October is considered as representative of the pre-HPE conditions.

3.2 Distribution of SWI over the Mediterranean

The moisture structure upstream of the HPE; 1) the presence of an African moisture plume favouring the efficiency of the convection to produce more precipitation, 2) the importance of southerly flow from the warmer Mediterranean Sea south of Sicily in enhancing the convergence ahead of the cold front, and 3) the role of the upper-level trough over southern France extending to the western Mediterranean in organizing convection at the leading edge of the surface front, highlighted by Lee et al. (2016) has been further studied using SWI data. At 16 UTC on 15 October 2012, an upper-level trough located over south-eastern France extends to northern Algeria. Sea-level pressure values lower than 1002 hPa can be observed over south-eastern France extending to northern Italy (Fig. 3a) with the associated cyclonic flow seen at 850 hPa. Strong northerly mistral and tramontane winds associated with cold and dry air, with $\delta^{18}O_v$ less than –16‰ and q less than 2 g kg^{-1} (Fig. 4a, b), and thus low potential temperature, θ, are located over the Gulf of Lion ($\leq$ 300 K, dark-blue area in Fig. 3b). Fig. 4a shows two bands of large q values in excess of 6 g kg^{-1} at 850 hPa upstream of the HPE, one over the Tyrrhenian Sea (‘TY’ box in Fig. 3b) where a cold front is located (large gradient of θ in range of 315–330 K, dashed line in Fig. 3b), and another one across north Africa extending towards SI with south to south-westerly winds where the African moist plume with the values of $\theta \geq 330$ K is located (red area in Fig. 3b), ahead of trough. At 600 hPa (Fig. 4c), $\delta^{18}O_v$ values in excess of −25 ‰ can be seen at the southern edge of the surface cold front. This signature can be explained by the transport of water vapour to higher levels by updrafts along the front. Another interesting point we can see by comparing the q with the $\delta^{18}O_v$ maps (crescent closed by dashed line, Fig. 4a−b) is that an additional band of enriched water vapour ($\delta^{18}O_v \geq -18$ ‰, Fig. 4b) is found at the southern boundary of the mistral (and the tramontane), in a region of still relatively low q values ($\leq$ 5 g kg^{-1}, Fig. 4a). This SWI-enriched band reflects the moisture brought to higher levels by convective updrafts that develop within the strong mistral outflow over the warm sea surface, typical of cold-air outbreaks. In this region, a band of moderate brightness temperature at 10.8 μm (230−240 K, altitudes about 5−6 km) is measured by the Spinning Enhanced Visible and Infrared Imager on board the geostationary Meteosat Second Generation satellite (not shown, see Fig. 4 of Lee et al., 2016). In the simulation, weak precipitation is also produced in this region from clouds located mostly below 5 km above sea level (ASL) (not shown).

The hourly evolution of the moist and SWI-enriched air mass over the TY during the period 16−20 UTC can also be seen in the hourly evolution of $\delta^{18}O_v$ in Fig. 5, which shows the average $\delta^{18}O_v$ in 1-km deep layers spanning from 1 to 7 km ASL in the TY region from 09 UTC on 15 October to 09 UTC on 16 October together with the average θ values at 850 hPa within TY. From 09 UTC to 19 UTC on 15 October, while the average θ value at 850 hPa is consistently high at 322 K, the $\delta^{18}O_v$ values between 1 and 5 km ASL slightly increase but the $\delta^{18}O_v$ values between 5 and 7 km ASL gradually decrease revealing the arrival of the upper-level trough (Figure 5a).

During the two precipitation phases at 20 UTC and 00 UTC, both θ and $\delta^{18}O_v$ drop dramatically (Figs. 5a) with the arrival of the upper-level trough cold front in the TY region (Figs. 3c–f, and 4d–i), while the warm and moist air mass with large q and large $\delta^{18}O_v$ values coming from tropical Africa persists upstream of SI (Fig. 5b). At 20 UTC (Fig. 3c, d), southerly winds (10−15 m s^{-1}) transport the warm and moist air mass with high θ values ($\geq$ 325 K) from the Strait of Sicily to SI, and the convection occurred in the high θ region at the southern edge of the front (dashed line in Fig. 3d). The frontal wind convergence of south-westerly and southerly winds (10−15 m s^{-1}) can be seen upstream of the HPE at the 850-hPa level.

Then at 00 UTC when the trough is located in the southern Tyrrhenian Sea with the low-level mistral air mass ($q \leq 3$ g kg^{-1} and $\delta^{18}O_v \leq -24$‰ in Fig. 4g–h) at the western edge, strong cyclonic flow can be identified over the SI region while the warm and moist air mass ($\theta \geq 325$ K) over the Strait of Sicily is continuously advected towards SI (Fig. 3f). Higher up, at 600 hPa, the trough-related, strongly SWI-depleted air masses descending from higher altitudes show $\delta^{18}O_v$ values lower than −45 ‰ (Fig. 4i). In contrast to the trough, the African moisture plume is associated with large q values in excess of 10 g kg^{-1} at 850 hPa level extending to the SI region (Fig. 4g). As θ decreases from 322 to 300 K in TY (Fig. 5a), the $\delta^{18}O_v$ drops more rapidly at altitudes above 3 km compared to the $\delta^{18}O_v$ drop seen in lower altitudes, where the trough-related dry airstreams are moistened by SWI-enriched fresh ocean evaporate. The minimum $\delta^{18}O_v$ value increases lowering the altitudes to near surface, for instance, the minimum $\delta^{18}O_v$ values of −23 and −36 ‰ are seen at 1−2 and 2−3 km ASL respectively, while values lower than −47 ‰ occur at altitudes above 3 km ASL. The hourly evolution of average $\delta^{18}O_v$ in the TY region shows the propagation of the surface front and upper-level trough at altitudes of 1−7 km ASL, and the associated subsidence of dry and cold air. It is worth noting that the arrival timing of cold and dry air subsidence in TY, 19−20 UTC, (Fig. 5a) corresponds to the onset of precipitation in SI, 19 UTC (vertical bars, Fig. 2). Overall the synoptic evolution simulated by COSMOiso is similar to the one analysed using an observational dataset by Lee et al. (2016).

4. SWI distribution during two precipitation phases

The temporal evolution of the domain-averaged $\delta^{18}O_v$ in water vapour and q within the SI area at the first model level (approximately 20 m ASL) (Fig. 6) shows the different behaviour during IOP 13. While the q value increases gradually to 13.5 g kg^{-1} until 19 UTC, just before P1, the $\delta^{18}O_v$ value maximizes to −13.6 ‰ at 16 UTC and then decreases during P1 to −15 ‰. During P2, the $\delta^{18}O_v$ value increases shortly to −14.6 ‰ whereas the q value continues to decrease to 8 g kg^{-1}. The detailed 3-D history and structure of $\delta^{18}O$ and q of the air parcels associated with P1 and P2 over SI will be shown in the following section.

4.1. The convective phase of precipitation

4.1.1. History of air parcels and related SWI evolution

This section aims to investigate the history of the air masses involved in the convective precipitation phase P1. Figure 7 displays the history of air parcel arriving at SI in the layer 800−700 hPa at 20 UTC on 15 October 2012. The 3-day backward trajectories shown in Fig. 7 indicate that the air parcels arriving in the SI region in the layer between 800 and 700 hPa at 20 UTC on 15 October are from the North Atlantic. These air parcels are mostly dry ($q \leq 5$ g kg^{-1}) along the track during the 3 days except for the last 18 hours before their arrival in SI (Fig. 7a). In the period between 48 and 18 hours before their arrival in SI the air parcels descend rapidly from altitudes of 3-5 km to below 1 km ASL over the Tyrrhenian Sea, and below 2.5 km ASL over the Strait of Sicily (Fig. 7d). This penetration of dry air from upper-levels to the surface enhances surface evaporation, leading to a sharp increase of q as well as $\delta^{18}O_v$ (Fig. 7a−c). Between 18 and 6 hours before arrival in SI, the median surface evaporation rate along the trajectories doubles from 0.15 to 0.32 mm h^{-1} with a peak 12 hour before the arrival in SI (Fig. 7c). A few air parcels travel over the Strait of Sicily towards SI where mixing with the moist and SWI-enriched moisture plume from North Africa occurs (Fig. 4d−f). The median q value along the trajectories increases by a factor of 2.5 from 3.8 to 8.4 g kg^{-1} with the peak 10 hour before arrival in SI, whereas the median $\delta^{18}O_v$ value increases from −27 to −18 ‰ (not shown).

Figure 8 displays the q–$\delta^{18}O_v$ scatter diagram along the entire trajectories seen in Fig. 7 at different times before their arrival at SI. Figure 8 also shows that the q and $\delta^{18}O_v$ values rapidly increase in the last 12 hours prior to arrival in SI. Between 60 and 12 hours before the arrival of the air parcels in SI (Fig. 8a, b), the q and $\delta^{18}O_v$ values are still relatively small, i.e. average q of 2−6 g kg^{-1}, average $\delta^{18}O_v$ between −25 and −19 ‰, in the dry pocket of the upper-level trough. During the last 12 hours (black star, Fig. 8b), q is about 9 g kg^{-1} on average, and the average δ^{18}O$_v$ is about −17 ‰. During this time, the q–δ^{18}O$_v$ evolution follows a curve that lies close to a typical Rayleigh line for the Mediterranean condition (SST of 26°C, blue line), indicating the onset of precipitation. Several points fall substantially below this Rayleigh distillation line (solid line, Fig. 8b), suggesting a precipitation recycling by partial re-evaporation of rain drops (Worden et al., 2007).

Between 6 and 3 hours before their arrival in SI, the upper to low-level trajectories (grey to purple dots in Fig. 9a, b) follow a mixing line (dashed line) during their descent while the lowermost trajectories (black and grey dots) partly follow a Rayleigh distillation line (solid line). This shows that the descending dry air parcels mix with the warm and moist air parcels from lower altitudes, which also increases surface evaporation. During P1 (Fig. 9c), the q–δ^{18}O$_v$ evolution at all levels lies on and below the Rayleigh line, suggesting that air parcels are representative of the convective updraft after condensation of the rain drops (q–δ^{18}O$_v$ along the Rayleigh curve) and that some air parcels took up the evaporated moisture from falling precipitation.

4.1.2. Horizontal distribution of SWIs

At 20 UTC, the precipitation feature over SI is associated with a region of enhanced convective activity and multiple convective cells extending from SI to the Strait of Sicily (area closed by dashed line in Fig. 10a) ahead of the surface cold front where westerly and north-westerly winds prevail at 542 m ASL (Fig. 10b) and the frontal south-westerly wind is dominant at 2455 m ASL (Fig. 10d). Within the precipitation area, relatively low δ^{18}O$_v$ values (≤ −16 ‰) than in the vicinity are found at 542 m ASL while relatively high δ^{18}O$_v$ values between −20 and −24 ‰ are found at 2455 m and 5565 m ASL, respectively (Fig. 10d, f), showing the signature of strong and deep convective mixing that brings SWI-depleted moisture towards the surface within the downdrafts and SWI-enriched moisture is pumped to higher altitudes within the updrafts. This signature is consistent with the temporal evolution of average δ^{18}O$_v$ in SI. Figure 5b shows a larger δ^{18}O$_v$ increase at high altitudes of 4−7 km ASL (green to purple lines in Fig. 5b) than at lower altitudes of 1−3 km ASL (black to yellow lines) from 19 to 22 UTC. The SWI-enriched air masses with high δ^{18}O$_r$ values in rain (≥ −10 ‰), are distributed over the TY region (Fig. 10e) and SWI-enriched air masses with high δ^{18}O$_s$ values in snow (≥ −16 ‰), are aligned ahead of the cold front over Sicily (Fig 10g). The depletion of water vapour and the enrichment of rain water and snow over the TY indicate the uptaking by the air mass of evaporated moisture from falling hydrometeors.

At the same time, the African moisture plume is associated with SWI-enriched vapour with large $\delta^{18}O_v$ in excess of −22 ‰ and SWI-enriched snow with values of $\delta^{18}O_s$ larger than −12 ‰ around the southern tip of the precipitating area at 5565 m (Fig. 10f, g), indicating the continuous supply of the enriched moisture plume from North Africa to SI. We can see this constantly large $\delta^{18}O_v$ values in SI at all altitudes between 1 and 7 km during IOP13 in Fig. 5b. The dry pocket of the upper-level trough is distinguished by SWI-depleted vapour air masses with low $\delta^{18}O_v \leq -36$ ‰ at 2455 m and 5565 m ASL over Sardinia and Corsica (Fig. 10d, f).

The Lagrangian analysis indicates that most of processes inducing precipitation during P1 take place during the last 18 hours over the Tyrrhenian Sea and the Strait of Sicily. The descending air parcels from the mid troposphere reach altitudes below 1 km ASL at the cold front and take up large amounts of evaporated moisture near the warm sea surface of the Tyrrhenian Sea. Then additional moisture is taken up at altitudes below 2 km ASL from mixing with the African moisture plume that extends from the African continent to the Strait of Sicily. During the period from 18 to 6 hour before the precipitation peak P1, the q and $\delta^{18}O_v$ values strongly increase. At the time of precipitation, strong convective mixing injects SWI-enriched moisture into higher altitudes and depleted moisture to near surface over SI.

4.2. The large-scale phase of precipitation

4.2.1. History of air parcel and related SWI evolution

The 3-day backward trajectories in Fig. 11 evidence that the air parcels arriving at SI in the layer between 800 and 700 hPa at 000 UTC on 16 October come from North Africa and partly from the southern Iberian Plateau. The air parcels are consistently moist along the tracks (Fig. 11a), with average q value mostly ≥ 5 g kg^{-1} along the track, in contrast to the air parcels involved in the P1 phase (see section 4.1.1). During the 3 days prior to their arrival in SI, the air parcels are enriched with SWI, showing large $\delta^{18}O_v$ values in excess of −24 ‰, and the air parcels are located at low altitudes mostly below 2 km ASL (Fig. 11b, d). They continuously take up water vapour over North Algeria and in the Strait of Sicily (Fig. 11a–b), and the median q increases from 6.5 to 9 g kg^{-1} and the median $\delta^{18}O_v$ increases from −18 to −16 ‰ in the period from 72 to 10 hours before the precipitation onset. The air parcels arriving at SI at 00 UTC at higher levels between 700 and 500 hPa are also moist and SWI-enriched, originate from North Africa (not shown), and are related to the moist tropical plume.

These moist and SWI-enriched air parcels are also evident from the scatter diagram of q and $\delta^{18}O_v$. Figure 12 shows the relatively large q and $\delta^{18}O_v$ values during the 3 days prior to their arrival in SI, i.e. q of

5−16 g kg^{-1} (average of 8−10 g kg^{-1}), and $\delta^{18}O_v$ between −12 and –25 ‰ (average in −16 and −18 ‰). During this period, the minimum $\delta^{18}O_v$ of the air parcel gradually increases from −33 to −27 ‰. In particular the moist branch of this q–$\delta^{18}O_v$ distribution lies close to Rayleigh distillation curve (solid line, Fig. 12a−c) for all 3 days, indicating sustained cloud and precipitation formation. As above, values below this Rayleigh curve point to the importance of precipitation recycling, which also occurs repeatedly during the 3-day period.

4.2.2. Horizontal distribution of SWIs

At 00 UTC on 16 Oct. during P2, stronger precipitation than that of P1 is produced, and the precipitation system is located mainly over SI (marked area closed by dashed line in Fig. 13a). In the vicinity of the precipitating region, strong cyclonic south-westerly flow ≥ 25 m s^{-1} is dominant at 2455 m and 5565 m ASL (Fig. 13d, f). Within the precipitating area, water vapour is gradually depleted and $\delta^{18}O_v$ values are relatively low from near the surface (542 m ASL) to mid altitudes of 5565 m ASL (Fig. 13b, d, and f). A strong depletion of isotopes in rain water is seen at 2455 m ASL (Fig. 13e). This is due to the steady large-scale ascent of air parcels in front of the trough that lead to cloud formation and rain out. The strong depletion of vapour in lower to mid altitudes is also evident from Fig. 5b, which shows decreasing $\delta^{18}O_v$ values from 23 to 01 UTC (black to purple lines). It is worth noting that θ increases continuously until 23 UTC and reaches 327 K in SI (thin line with white circles in Fig. 5b), while θ is rather constant before the arrival of the front and trough and the peak value is about 5 K lower in TY compared to SI (thin line with white circles in Fig. 5a, b). This reflects the influence of the moisture plume from North Africa. The moist and enriched African moisture plume including high $\delta^{18}O_v$ of vapour in excess of −22 ‰ is advected by the strong south-westerly flow from the Strait of Sicily to SI (Fig. 13d). This is consistent with the rapid re-enrichment of vapour in SI after the precipitation (Fig. 5b). Then after 04 UTC, with the arrival of the front and upper-level trough, the vapour becomes more depleted at all levels (Fig. 5b).

The Lagrangian analysis indicates that the moistures that feeds the convection during P2 is coming from North Africa and the air parcels take up additional moisture (2−3 g kg^{-1}) over the Mediterranean. These air parcels carry moist and SWI-enriched air at layers below 2 km ASL. With the arrival of the upper-level trough over the southern Tyrrhenian Sea, strong cyclonic flow leads to the mixing of air from the African moist plume to SI. During P2, the gradual depletion of water vapour takes a place at SI at all levels.

5. Conclusion

On 15 to 16 October 2012, SI experiences a HPE (total precipitation of 62.4 mm) with two phases of precipitation. The first one (P1) is induced by moist convection, while the second one (P2) is mainly associated with large-scale uplift along a front. The moisture transport and processes responsible for the HPEs that occurred over the SI area during IOP 13 have been analysed here using SWI data obtained from a numerical simulation with COSMO$_{\mathrm{iso}}$ at 7-km horizontal resolution. The main findings are summarized in two schematic illustrations (Fig. 14).

The 3-day backward trajectory analysis shows that the air parcels arriving in SI during P1 originate from the North Atlantic and descend within the upper-level trough over the north-western Mediterranean Sea. The SWI-depleted air mass (median δ^{18}O ≤ -45 ‰) within the descending air parcels rapidly take up a large amount of water vapour from ocean evaporation (green encapsulated area in Fig. 14a) over the Tyrrhenian Sea and also from evaporated moisture from falling precipitation. Additional moisture is taken up over the Strait of Sicily from mixing with the enriched moisture plume coming from Africa ($\delta^{18}O_v \geq -16$ ‰). The SWI-enriched low-level air masses arriving upstream of SI are convectively pumped to higher altitudes, producing precipitation over SI, and the SWI-depleted moisture is transported towards the surface within the downdrafts ahead of the cold front (red and blue arrows, Fig. 14a).

During P2 (Fig. 14b), just a few hours after P1, the origin of the air parcels arriving at SI is distinct, i.e. mostly from North Africa. The air parcels are moist and associated with large δ^{18}O values (bottom most arrow, median $\delta^{18}O_v \geq -16$ ‰). With the arrival of the upper-level trough ($\delta^{18}O_v \leq -45$ ‰) and mistral ($\delta^{18}O_v \leq -25$ ‰) over the southern Tyrrhenian Sea, the strong cyclonic flow around the trough (grey dashed line in Fig. 14b) induces the advection of the moist plume towards SI and leads to large-scale uplift of the warm and moist African air mass along the cold front. It brings moisture and leads to gradual rain out of the air parcels over Italy. For the convective precipitation phase (P1), most of the moisture processes producing the HPE take place during the last 18 hours before the arrival over SI, while the large-scale advection of SWI-enriched moisture from the African plume by strong cyclonic flow lasts about 72 hours during the large-scale precipitation phase (P2). In both phases, the air parcels take up substantial amount of water vapour over the Mediterranean.

Using the hourly 3-D water vapour isotope data, we highlight the large variety of moisture sources and transport pathways that induced the two phases of the HPE in South Italy during IOP13, and the isotopic characteristics of various air masses associated with the upper-level trough, cold front, mistral, and African moist plume, that were involved in convection development. We also highlight the role of the upper-level trough over the south Tyrrhenian Sea in driving the advection of the SWI-enriched plume from North Africa into the region of the deep convective system resulting in heavy precipitation over SI. Moreover, we demonstrate the importance of various moist processes such as mixing, condensation, and re-evaporation along the pathway based on the q–δ analysis using 3D SWI fields. Although our study is entirely based on a model simulation, the results suggest that the information on mesoscale moist dynamical processes and moisture transport that is contained in SWI, when combined with SWI observations, can provide very useful constrains on the representation of such processes in numerical models.

Our study is the first study to investigate the potential benefit of SWI in the context of a HPE in the Mediterranean. As such, our study provides a proof of concept of the usefulness of SWI data to understand the variety of origins and moist processes associated with air masses feeding the convection over SI. This will be further investigated in future research using SWI measurements obtained from various platforms, e.g. ground-based, near surface, airborne (Sodemann et al., 2017), and space-borne. Our modelling study will also allow designing forthcoming tailored field campaigns in the Mediterranean region. In this study, COSMOiso simulation at a horizontal grid spacing of about 7 km with parameterized convection results from a trade-off between having high enough resolution for including detailed dynamics of the mesoscale systems and being able to run efficiently over a large domain (about 4,300 km × 3,500 km) that includes the moisture plume over North Africa. This setup allows addressing the question we are interested in, namely: which isotope signals are due to local processes, and which are due to large-scale advection? To further study the details of the fractionation processes in and around deep convective systems, complementary investigations will be conducted using higher resolution convection-permitting simulation with a 2 km grid to shed a light on cloud microphysical processes inside deep convection.

Author contribution

KOL, FA, SP and CF planned the manuscript and analyses. SP and KOL designed the numerical simulation and SP performed it. JLL and JPC contributed to discussion. KOL prepared the manuscript with contributions from all co-authors.

Acknowledgements

This work was supported by the French Agence Nationale de la Recherche (ANR) via the IODA-MED Grant ANR-11-BS56-0005, the MUSIC grant ANR-14-CE01-014 and the MISTRALS/HyMeX programme.

References

Aemisegger, F. and Papritz, L.: A climatology of strong large-scale ocean evaporation event. Part I: Identification, global distribution, and associated climate conditions. J. Climate, 31, 7287–7312, doi:10.1175/JCLI-D-17-0591.1, 2018.

Aemisegger, F., Spiegel, J. K., Pfahl, S., Sodemann, H., Eugster, W., and Wernli, H.: Isotope meteorology of cold front passages: A case study combining observations and modelling. Geophys. Res. Lett., 42, 5652−5660, doi:10.1002/2015GL063988, 2015.

Aemisegger, F. and Sjolte, J.: A climatology of strong large-scale ocean evaporation event. Part II: Relevance for the deuterium excess signature of the evaporation flux. J. Climate, 31, 7313–7336, doi:10.1175/JCLI-D-17-0592.1, 2018.

Barthlott C, Davolio S. 2015. Mechanisms initiating heavy precipitation over Italy during the HyMeX Special Observation Period 1: A numerical case study using two mesoscale models. *Q. J. R. Meteorol. Soc.* DOI: 10.1002/qj.2630.

Blossey, P. N., Huang, Z., and Romps, D. M.: Isotopic composition of water in the tropical tropopause layer in cloud-resolving simulations of an idealized tropical circulation, J. Geophys. Res., 115, D24309, doi: 10.1029/2010JD014554, 2010.

Bonne, J. L., Masson-Delmotte, V., Cattani, O., Delmotte, M., Risi, C., Sodemann, H., and Steen-Larsen, H. C.: The isotopic composition of water vapor and precipitation in Ivittuut, southern Greenland, Atmos. Chem. Phys., 14(9), 4419–4439, 2014.

Christner, E., Aemisegger, F., Pfahl, S., Werner, M., Cauquoin, A., Schneider, M., Hase, F., Barthlott, S., and Schädler, G.: The climatological impacts of continental surface evaporation, rainout, and subcloud processes on δD of water vapor and precipitation in Europe. Journal of Geophysical Research: Atmospheres, 123, 4390–4409. https://doi.org/10.1002/2017JD027260, 2018.

Davies, H. C.: A lateral boundary formulation for multi-level prediction models, Q. J. Roy. Meteor. Soc., 102, 405−418, 1976.

Dessler, A., and Sherwood, S.: A model of HDO in the tropical tropopause layer, Atmos, Chem, Phys., 3, 4489–4501, 2003.

Doms, G., Förstner, J., Heise, E., Herzog, H. J., Raschendorfer, M., Schrodin, R., Reinhardt, T., and Vogel, G.: A description of the nonhydrostatic regional model LM. Part II: Physical parameterization, Deutscher Wetterdienst, Offenbach, Germany, 2005.

Ducrocq, V., Braud, I., Davolio, S., Ferretti, R., Flamant, C., Jansa, A., Kalthoff, N., Richard, E., Taupier-Letage, I., Ayral, P.A., Belamari, S., Berne, A., Borga, M., Boudevillain, B., Bock, O., Boichard, J. L., Bouin, M. N., Bousquet, O., Bouvier, C., Chiggiato, J., Ciimini, D., Corsmeier, U., Coppola, L., Cocquerez, P., Defer, E., Delanoë, J., Di Girolamo, P., Doerenbecher, A., Drobinski, P., Dufournet, Y., Fourrié, N., Gourley, J.J., Labatut, L., Lambert, D., Le Coz, J., Marzano, F.S., Molinié, G., Montani, A., Nord, G., Nuret, M., Ramage, K., Rison, W., Roussot, O., Said, F., Schwarzenboeck, A., Testor, P., Van Baelen, J., Vincendon, B., Aran, M., and Tamayo, J.: HyMeX-SOP1: The Field Campaign Dedicated to Heavy Precipitation and Flash Flooding in the Northwestern Mediterranean. Bull. Am. Meteorol. Soc. 95, 1083−1100, doi:10.1175/BAMS-D-12-00244.1, 2014.

Duffourg, F. and Ducrocq, V.: Assessment of the water supply to Mediterranean heavy precipitation: A method based on finely designed water budgets. Atmos. Sci. Lett. 14, 133−138, 2013.

Duffourg, F., Lee, K. O., Ducrocq, V., Flamant, C., Chazette, P., and Girolamo, P. D.: Role of moisture patterns in the backbuilding formation of HyMeX IOP13 heavy precipitation system, Q. J. Roy. Meteor. Soc., 144: 291−303, doi:10.1002/qj.3201, 2018.

Dütsch, M., Pfahl, S., Meyer, M., and Wernli, H.: Lagrangian process attribution of isotopic variations in near-surface water vapour in a 30-year regional climate simulation over Europe. Atmos. Chem. Phys., 18, 1653–1669, https://doi.org/10.5194/acp-2017-744, 2018

Galewsky, J., and Hurley, J. V.: An advection-condensation model for subtropical water vapor isotopic ratios. J. Geophys. Res., 115, D16116, doi:10.1029/2009JD013651, 2008.

Galewsky, J., Steen-Larsen, H. C., Field, R. D., Worden, J., Risi, C., and Schneider, M.: Stable isotopes in atmospheric water vapor and applications to the hydrologic cycle. Rev. Geophys., 54, doi: 10.1002/2015RG000512, 2012.

Jacob, J. and Sonntag, C.: An 8-year record of the seasonal variation of ^{2}H and ^{18}O in atmospheric water vapour and precipitation at Heidelberg, Germany, Tellus B, 43, 291−300, doi:10.1034/j.1600-0889.1991.t01-2-00003.x, 1991.

Jaussaume, J., Sadourny, R., and Jouzel, J.: A general circulation model of water isotope cycles in the atmosphere, Nature, 311, 24−29, 1984.

Jouzel, J., Masson-Delmotte, V., Stiévenard, M., Landais, A., Vimeux, F., and Johnsen S. J.: Sveinbjornsdottir and White J.W.C., Rapid deuterium excess changes in Greenland ice cores: a link between the ocean and the atmosphere, CRAS, 337, 957-969, 2005.

Lacour, J. L., Flamant, C., Risi, C., Clerbaux, C., and Coheur, P. F.: Importance of the Saharan heat low in controlling the north Atlantic free tropospheric humidity budget deduced from IASI δD observation. Atmos. Chem. Phys., 17, 9645−9663, 2017.

Lee, K. O., Flamant, C., Ducrocq, V., Duffourg, F., Fourrié, N., and Davolio, S.: Convective initiation and maintenance processes of two back-building mesoscale convective systems leading to heavy precipitation events in Southern Italy during HyMeX IOP 13. Q. J. R. Meteorol. Soc, 142, 2623−2635, doi: 10.1002/qj.2978, 2016.

Lee, K. O., Flamant, C., Ducrocq, V., Duffourg, F., Fourrié, N., Delanoë, J., and Bech, J.: Initiation and development of a mesoscale convective system in the Ebro River Valley and related heavy precipitation over northeastern Spain during HyMeX IOP15a. Q. J. R. Meteorol. Soc, 143, 942−956, doi: 10.1002/qj.2851, 2017.

Lee, K. O., Flamant, C., Duffourg, F., Ducrocq, V., and Chaboureau, J.-P.: Impact of upstream moisture structure on a back-building convective precipitation system in south-eastern France during HyMeX IOP 13. Atmos. Chem. Phys., Discuss, http://doi.org/10.5194/acp-2018-707, 2018.

Lin, Y. L., Chiao, S., Wang, T. A., Kaplan, M. L., and Weglarz, R. P.: Some common ingredients for heavy orographic rainfall. *Wea. Forecasting,* 16, 633−660, 2001.

Martius, O., Zenklusen, E., Schwierz, C., and Davies, H. C.: Episodes of Alpine heavy precipitation with an overlying elongated stratospheric intrusion: A climatology. Int. J. Climatol. 26, 1149−1164, doi: 10.10002/joc.1295, 2006.

Noon, D.: The influence of midlatitude and tropical overturning circulation on the isotopic composition of atmospheric water vapor and Antarctic precipitation. J. Geophys. Res., 113, D04102, doi:10.1029/2007JD008892, 2008.

Noon, D.: Pairing measurement of the water vapor isotope ratio with humidity to deduce atmospheric moistening and dehydration in the tropical midtroposphere. J. Climate, 25, 4476−4494, doi: 10.1175/JCLI-D-11-00582.1, 2012.

Nuissier, O., Ducrocq, V., Ricard, D., Lebeaupin, C., and Anquetin, S.: A numerical study of three catastrophic precipitating events over southern France. I: Numerical framework and synoptic ingredients. Q. J. R. Meteorol. Soc. 134, 111−130, 2008

Nuissier, O., Joly, B., Joly, A., Ducrocq, V., and Arbogast, P.: A statistical downscaling to identify the large-scale circulation patterns associated with heavy precipitation events over southern France. Q. J. R. Meteorol. Soc. 137, 1812−1827. doi:10.1002/qj.866, 2011.

Pfahl, S. and Wernli, H.: Air parcel trajectory analysis of stable isotopes in water vapor in the eastern Mediterranean, J. Geophys. Res., 113, D20104, doi: 10.1029/2008JD009839, 2008.

Pfahl, S., Wernli, H., and Yoshimura, K.: The isotopic composition of precipitation from a winter storm – a case study with the limited-area model COSMOiso. Atmos. Chem. Phys., 12, 1629−1648, doi: 10.5194/acp-12-1629-2012, 2012.

Ricard, D., Ducrocq, V., and Auger, L.: A climatology of the mesoscale environment associated with heavily precipitating events over a northwestern mediterranean area. J. Appl. Meteorol. Climatol. 51, 468−488. doi:10.1175/JAMC-D-11-017.1, 2012.

Risi, C., Bony, S., and Vimeux, F.: Influence of convective processes on the isotopic composition (O18 and D) of precipitation and water vapour in the Tropics: Part 2: Physical interpretation of the amount effect. J. Geophys. Res. 113, 2008.

Risi, C., Bony, S., Vimeux, F., Chong, M., and Descroix, L.: Evolution of the water stable isotopic composition of the rain sampled along Sahelian squall lines, Q. J. R. Meteorol. Soc., 136: 227−242, doi:10.1002/qj.485, 2010.

Röhner, L., Nerding, K.-U., and Corsmeier, U.: Diagnostic study of a HyMeX heavy precipitation event over Spain by investigation of moisture trajectories. Q. J. R. Meteorol. Soc., 142 (Suppl 1): 287−297, doi:10.1002/qj.2825

Schneider, M., Wiegele, A., Barthlott, S., González, Christner, E., Dyroff, C., García, O. E., Hase, F., Blumenstock, T., Sepúlveda, E., Tsidu, G. M., Kenea, S. T., Rodríguez, and Andrey, J.: Accomplishments of the MUSICA project to provide accurate, long-term, global and high-resolution observations of tropospheric {H2O, δD} pairs – a review, Atmos. Meas. Tech., 9, 2845−2875, 2016.

Sherwood, S., and Dessler, A.: On the control of stratospheric humidity, Geophys, Res, Lett, 27(16), 2513–2516, 2000.

Sodemann, H., Aemisegger, F., Pfahl, S., Bitter, M., Corsmeier, U., Feuerle, T., Graf, P., Hankers, R., Jsiao, G., Schulz, H., Wieser, A., and Wernli, H.: The stable isotopic composition of water vapour above Corsica during the HyMeX SOP1 campaign: insight into vertical mixing processes from lower-tropospheric survey flights. Atmos. Chem. Phys., 17, 6125−6151, 2017.

Sprenger, M. and Wernli, H.: The LAGRANTO Lagrangian analysis tool – version 2.0, Geosci. Model Dev., 8, 2569-2586, 2015.

Steppeler, J., Doms, G., Schättler, U., Bitzer, H. W., Gassmann, A., Damrath, U., and Gregoric, G.: Meso-gamma scale forecast using the nonhydrostatic model LM, Meteorol. Atmos. Phys., 82, 75−96, 2003.

Sturm, K., Hoffmann, G., Langmann, B., and Stichler, W.: Simulation of delta O-18 in precipitation by the regional circulation model REMOiso, Hydrol. Process, 19, 3425−3444, doi:10.1002/hyp.5979, 2005.

Tiedtke, M.: A comprehensive mass flux scheme for cumulus parameterization in large-scale models, Mon. Weather Rev., 117, 1779−1800, 1989.

Tremoy, G., Vimeux, F., Soumana, S., Souley, I., Risi, C., Favreau, G., and Oi, M.: Clustering mesoscale convective systems with laser-based water vapor delta O-18 monitoring in Niamey (Niger), J. Geophys. Res., 119, 5079−5103, doi:10.1002/2013jd020968, 2014.

Turato, B., Reale, O., and Siccardi, F.: Water vapour sources of the October 2000 Piedmont flood. *J. Hydrometeorol.* 5, 693−712, doi:10.1175/1525-7541(2004)005<0693:WVSOTO>2.0CO;2, 2004.

Vimeux, F., Masson, V., Jouzel, J., Petit, J., Steig, E., Stievenard, M., Vaikmae, R. and White, J. W. C.: Holocene hydrological cycle changes in southern hemisphere documented in Antarctic deuterium excess records, Climate Dynamics, 17/7, 503−513, 2001.

Wernli, H. and Davies, H. C.: A Lagrangian-based analysis of ex- tratropical cyclones. I: The method and some applications, Q. J. R. Meteorol. Soc, 123, 467–489, 1997.

Winschall, A., Pfahl, S., Sodemann, H., and Wernli, H.: Impact of north Atlantic evaporation hot spots on southern Alpine heavy precipitation events. Q. J. R. Meteorol. Soc. 138, 1245−1258, doi: 10.1002/qj.987, 2012.

Winschall, A., Sodemann, H., Pfahl, S., and Wernli, H.: How important is intensified evaporation for Mediterranean precipitation extremes? J. Geophys. Res. Atmos. 119, 5240–5256, 2014.

Worden, J., Noone, D., Bowman, K., and Beer, R.: Importance of rain evaporation and continental convection in the tropical water cycle, Nature, 445, 528–532, 2007.

Yoshimura, K., Kanamitsu, M., Noone, D., and Oki, T.: Historical isotope simulation using Reanalysis atmospheric data, J. Geophys. Res., 113, D19108, doi:10.1029/2008JD010074, 2008.

Yoshimura, K., Kanamitsu, M., and Dettinger, M.: Regional downscaling for stable water isotopes: A case study of an atmospheric river event, J. Geophys. Res., 115, D18114, doi:10.1029/2010JD014032, 2010.

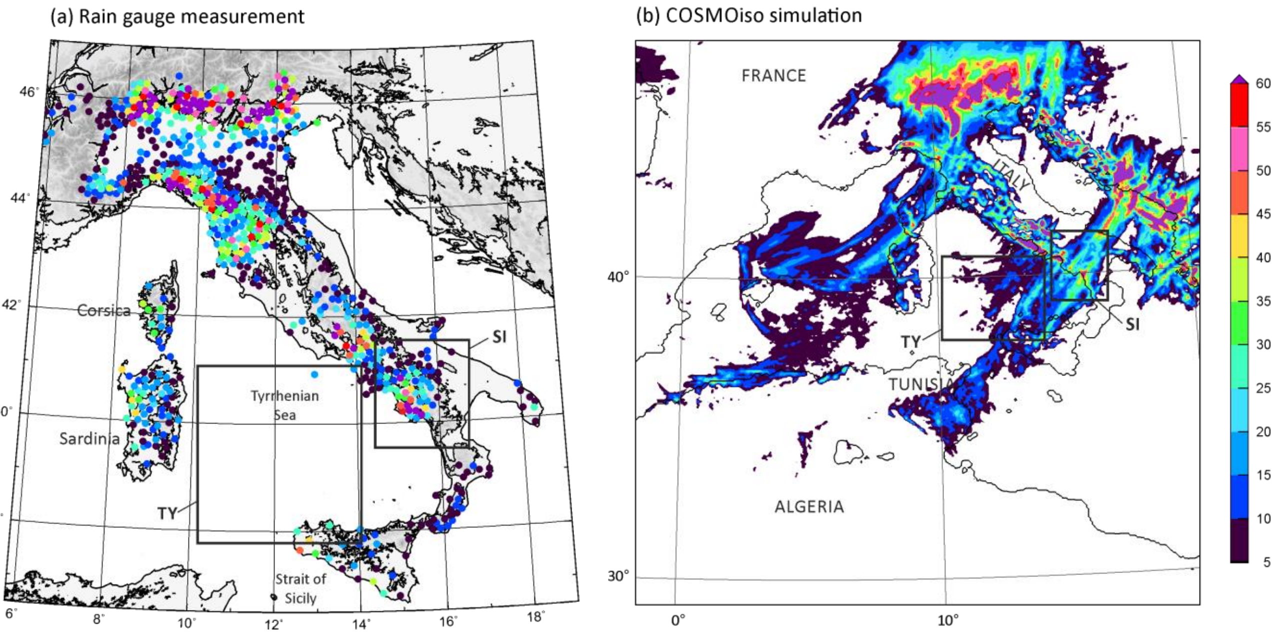

Figure 1. Accumulated precipitation during IOP 13 from 00 UTC on 15 October 2012 to 03 UTC on 16 October 2012 obtained from (a) rain gauge network, and (b) COSMOiso simulation.

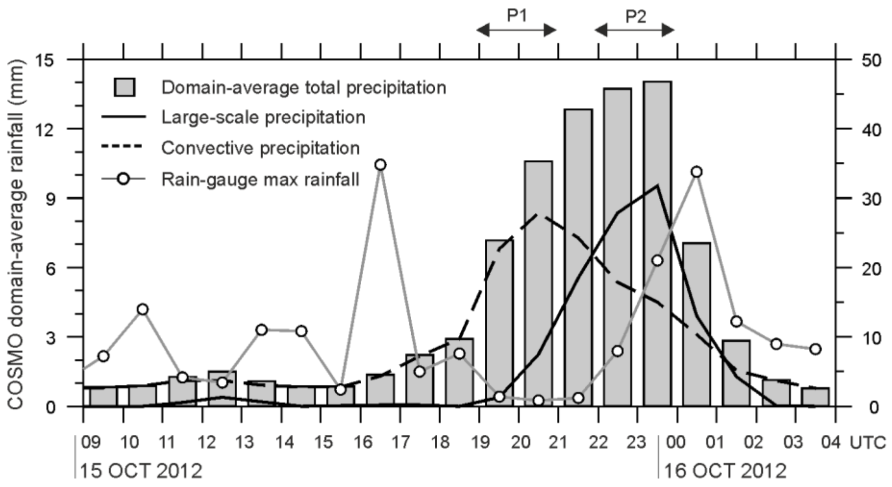

Figure 2. COSMOiso-produced domain-averaged total precipitation (bar), synoptic precipitation (black solid line), and convective precipitation (dashed line) in domain of South Italy (**SI**) over the land during IOP 13. Temporal evolution of observed maximum rainfall within the SI domain is shown by a line with dot. The location of domain SI is depicted by the box in Figure 1.

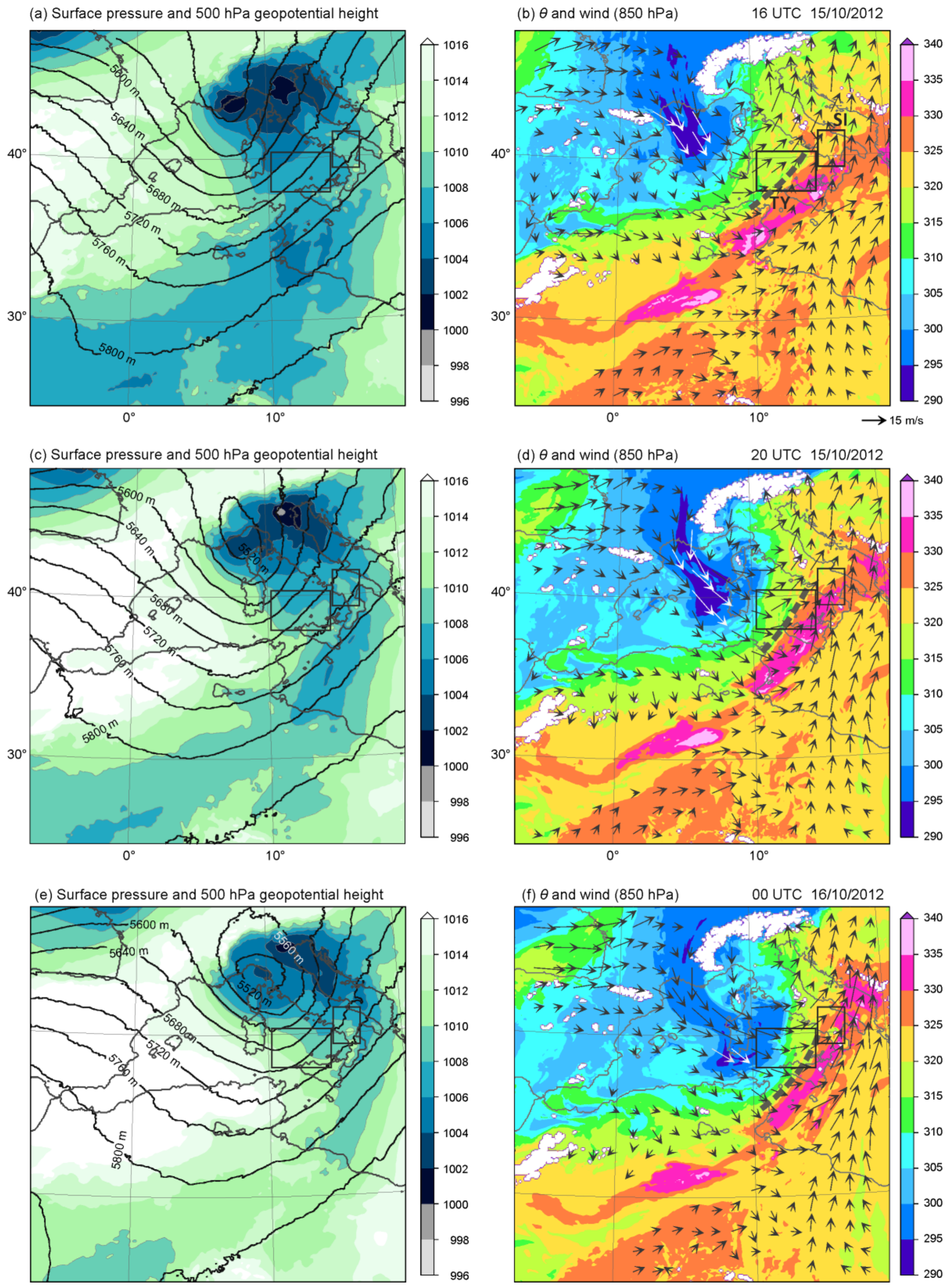

Figure 3. Horizontal distributions of sea level pressure (shades) and geopotential height at 500 hPa (contour) (left), and potential temperature, θ (shades), and wind (black and white arrows) at 850 hPa (right) at 16 UTC (top) and at 20 UTC (middle) 15 October 2012, and 00 UTC on 16 October 2012 (bottom) produced by the COSMOiso simulation. Coastal line is depicted by black line. The location of cold front is depicted by a dashed line in right panels.

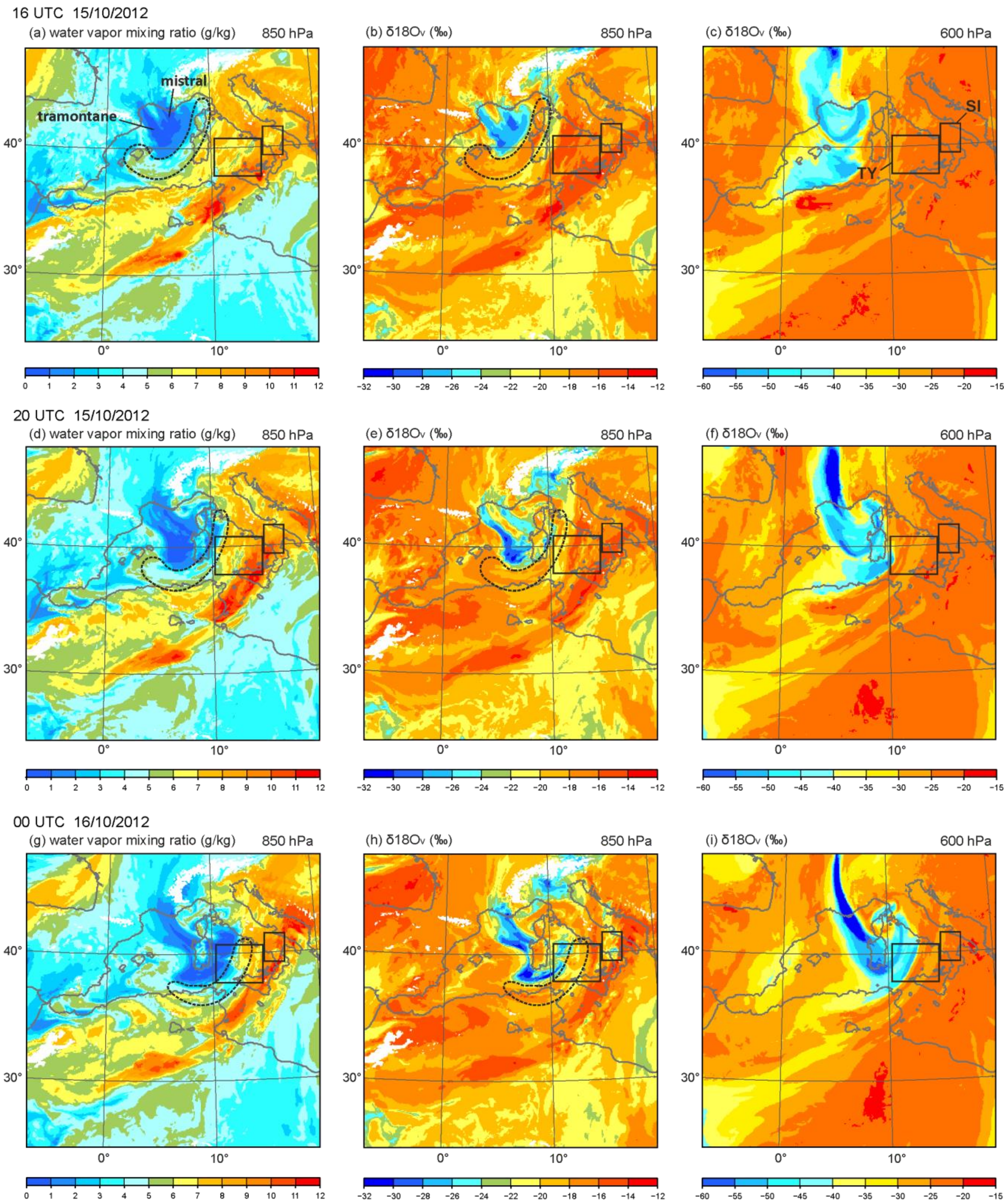

Figure 4. Horizontal distributions of water vapour mixing ratio at 850 hPa (left), $\delta^{18}O_v$ at 850 hPa (middle) and $\delta^{18}O_v$ at 600 hPa (right) at 16 UTC (top) and 20 UTC (middle) on 15 October 2012, and 00 UTC on 16 October 2012 (bottom).

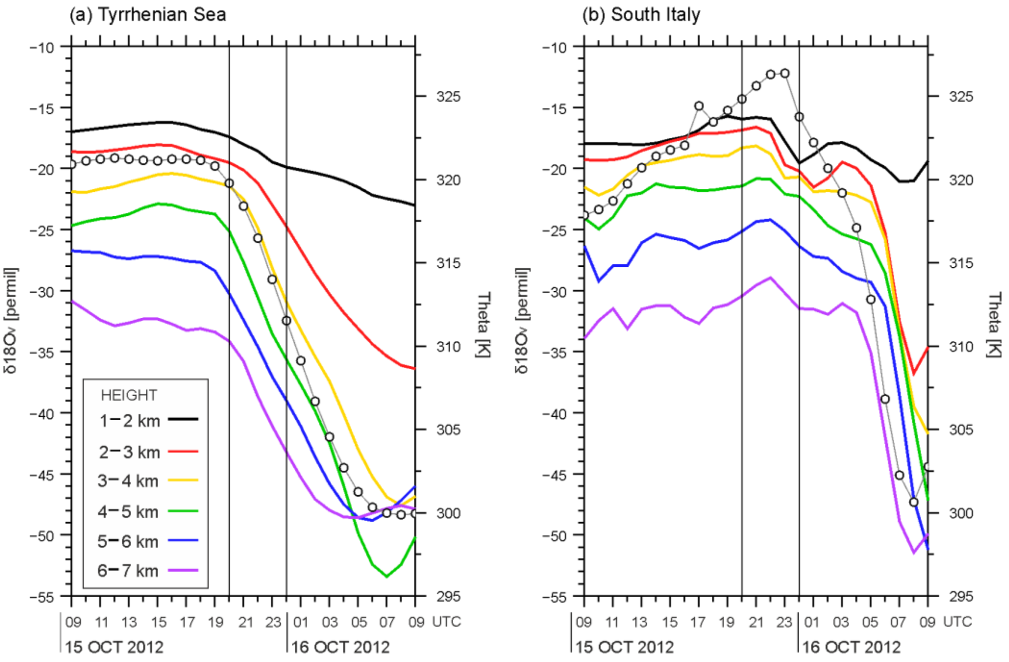

Figure 5. The averaged values of potential temperature (θ, K) at 850 hPa (thin line with dot) and $\delta^{18}O_v$ (‰) at altitudes of 1−2 km ASL (black), 2−3 km ASL (red), 3−4 km ASL (yellow), 4−5 km ASL (green), 5−6 km ASL (blue), 6−7 km ASL (purple) over the sea surface upstream the HPE of IOP 13 within domains of (a) Tyrrhenian Sea (marked by 'TY' in Figures 1, 3 and 4) and (b) South Italy (marked by 'SI') from 09 UTC on 15 October 2012 to 09 UTC on 16 October 2012.

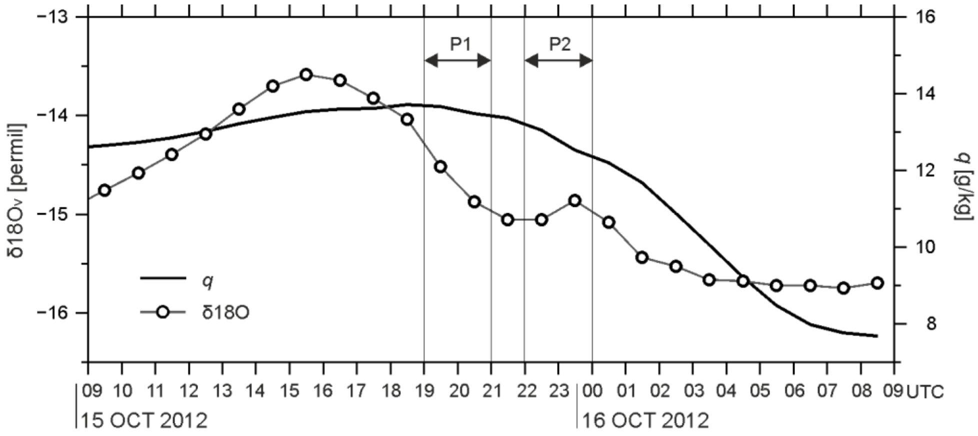

Figure 6. Domain-averaged $\delta^{18}O_v$ (line with dot) and q (thick line) in domain of South Italy (**SI**) at the first model level (approximately 20 m height) (limited to the grid point where the topography is lower than 20 m), from 09 UTC on 15 October 2012 to 09 UTC on 16 October 2012. The location of domain SI is depicted by the box in Figures 1 3, and 4.

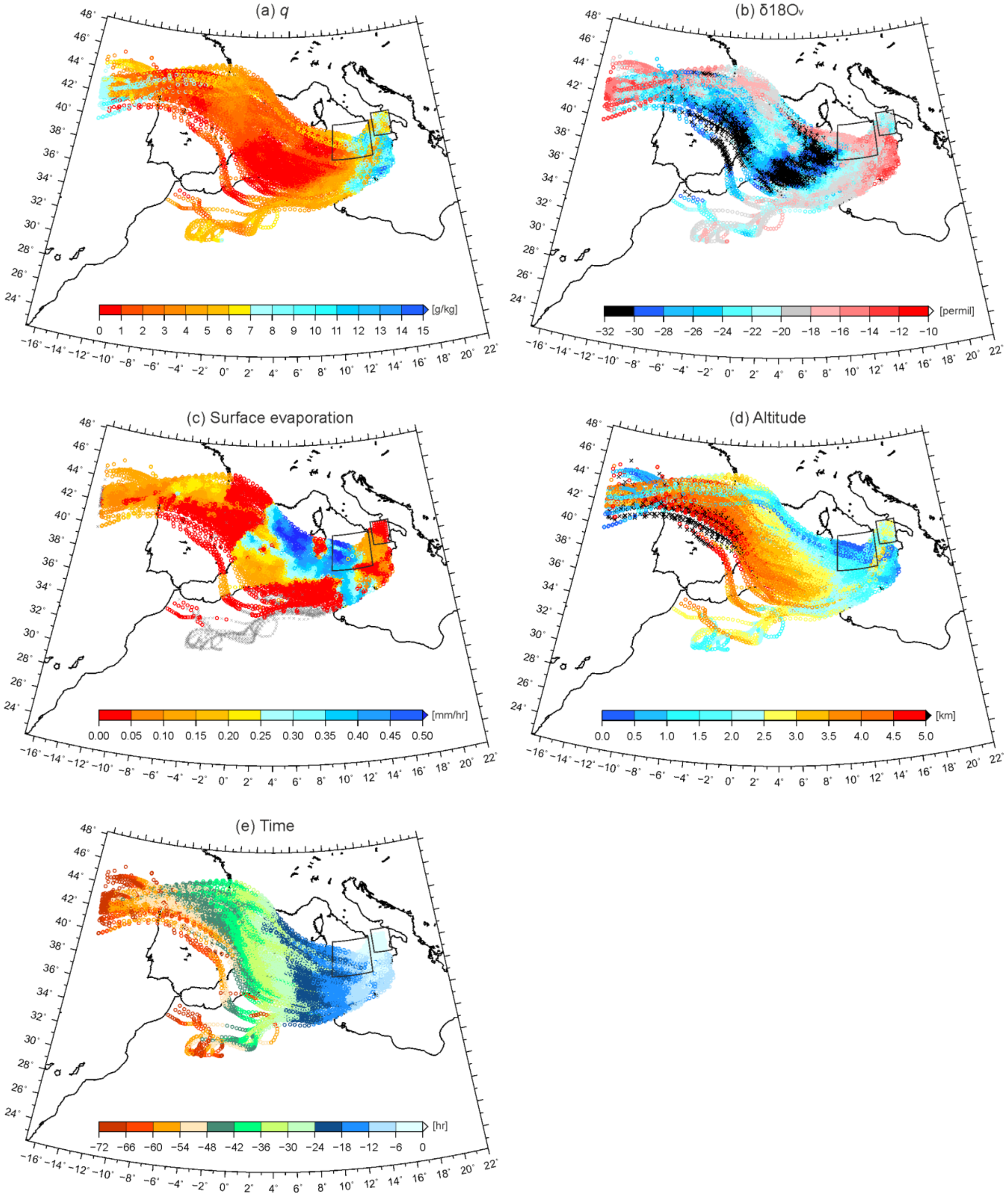

Figure 7. History of air parcel arriving at **SI** in layer of 800−700 hPa at 20 UTC on 15 October 2012. (a) water vapour mixing ratio, *q* (g kg^{-1}), (b) $\delta^{18}O_v$ (‰), (c) surface evaporation (mm h^{-1}), (d) altitude (km), and (e) time (h).

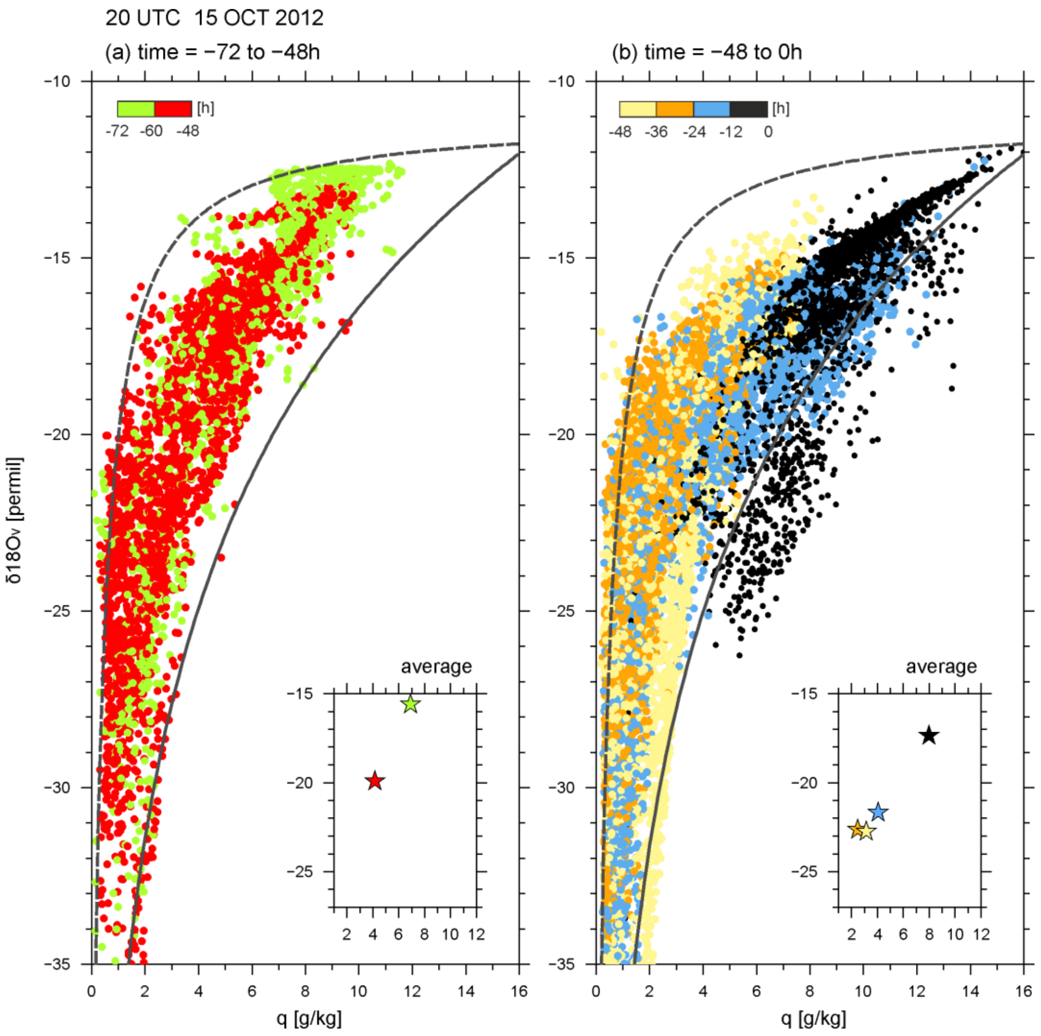

Figure 8. Scatter diagram of q and $\delta^{18}O_v$ along the backward trajectories of Figure 7 during (a) the times between −72 and −48 h, and (b) times between −48 and 0 h every 12 hours from 20 UTC on 15 October 2012. The colour of dot changes every 12 h. The mixing and Rayleigh lines are indicated in each panel by dashed and solid line, respectively. The averaged q and $\delta^{18}O_v$ every 12 hours is displayed in the bottom right corner of each panel.

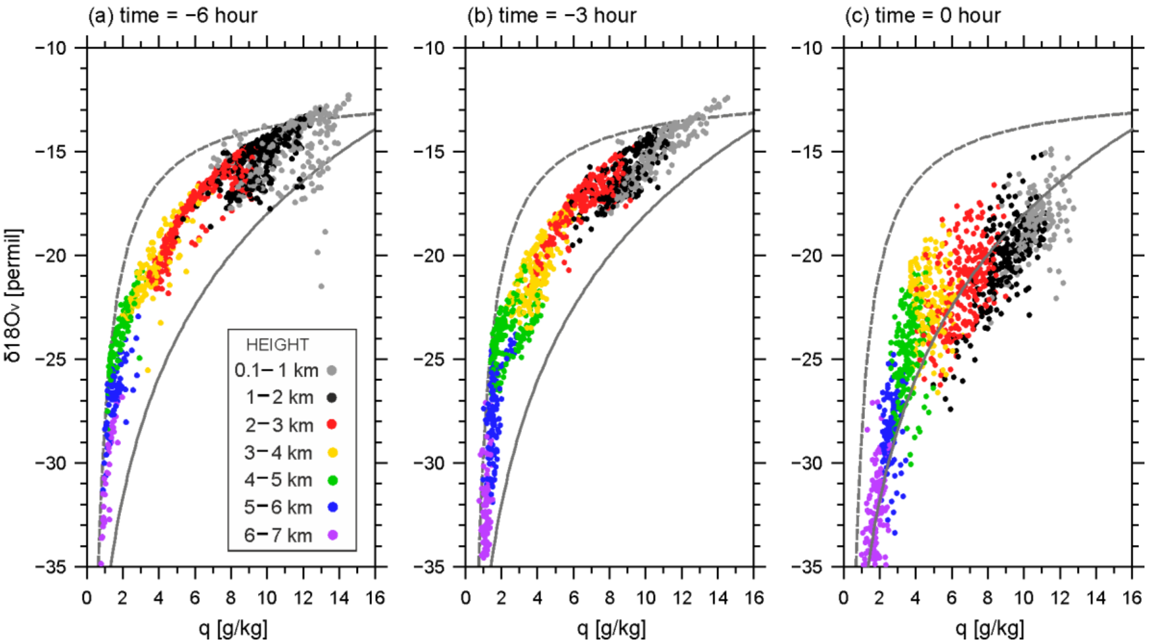

Figure 9. Scatter diagram of q and $\delta^{18}O_v$ along the backward trajectories of Figure 7 but for all altitudes of 1−2 km (black dots), 2−3 km (red dots), 3−4 km (yellow dots), 4−5 km (green dots), 5−6 km (blue dots), and 6−7 km (purple dots) at (a) −6 h, (b) −3 h, and (c) 0 h from 20 UTC on 15 October 2012. The mixing and Rayleigh lines are indicated in each panel by dashed and solid line, respectively.

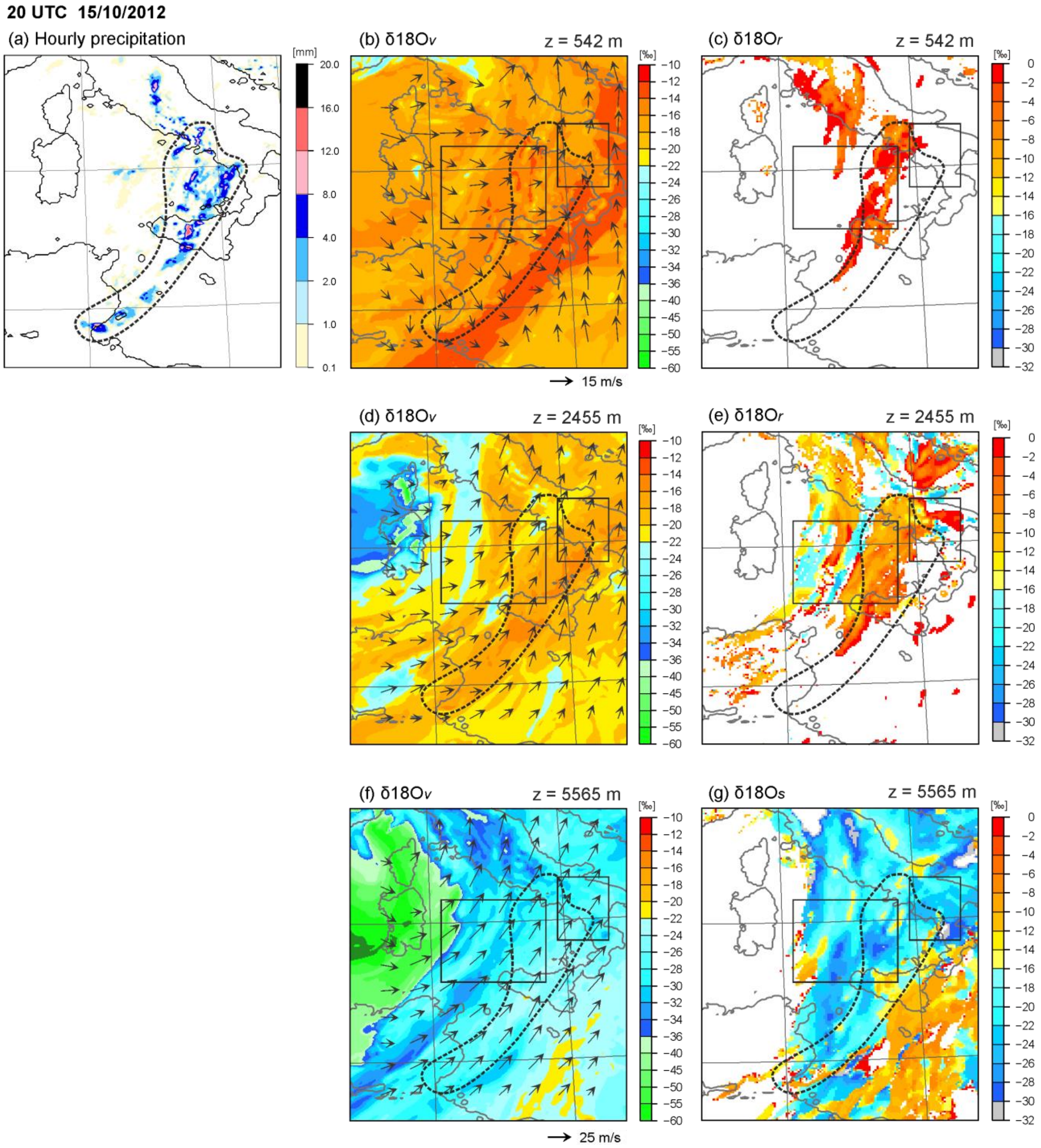

Figure 10. Horizontal distributions of (a) surface hourly precipitation (mm), $\delta^{18}O_v$ (‰) at (b) model level 8 (about 542 m ASL), (c) model level 16 (about 2455 m ASL), and (d) model level 23 (about 5565 m ASL, $\delta^{18}O_r$ (‰) at (e) 542 m ASL and (f) 2455 m ASL, and $\delta^{18}O_s$ (‰) at 5565 m ASL at 20 UTC on 15 October 2012. Note that due to the terrain-following coordinates, the SWI values are partly depleted over the topography, e.g. in central Italy. The precipitating area is marked by the area enclosed by the dashed line.

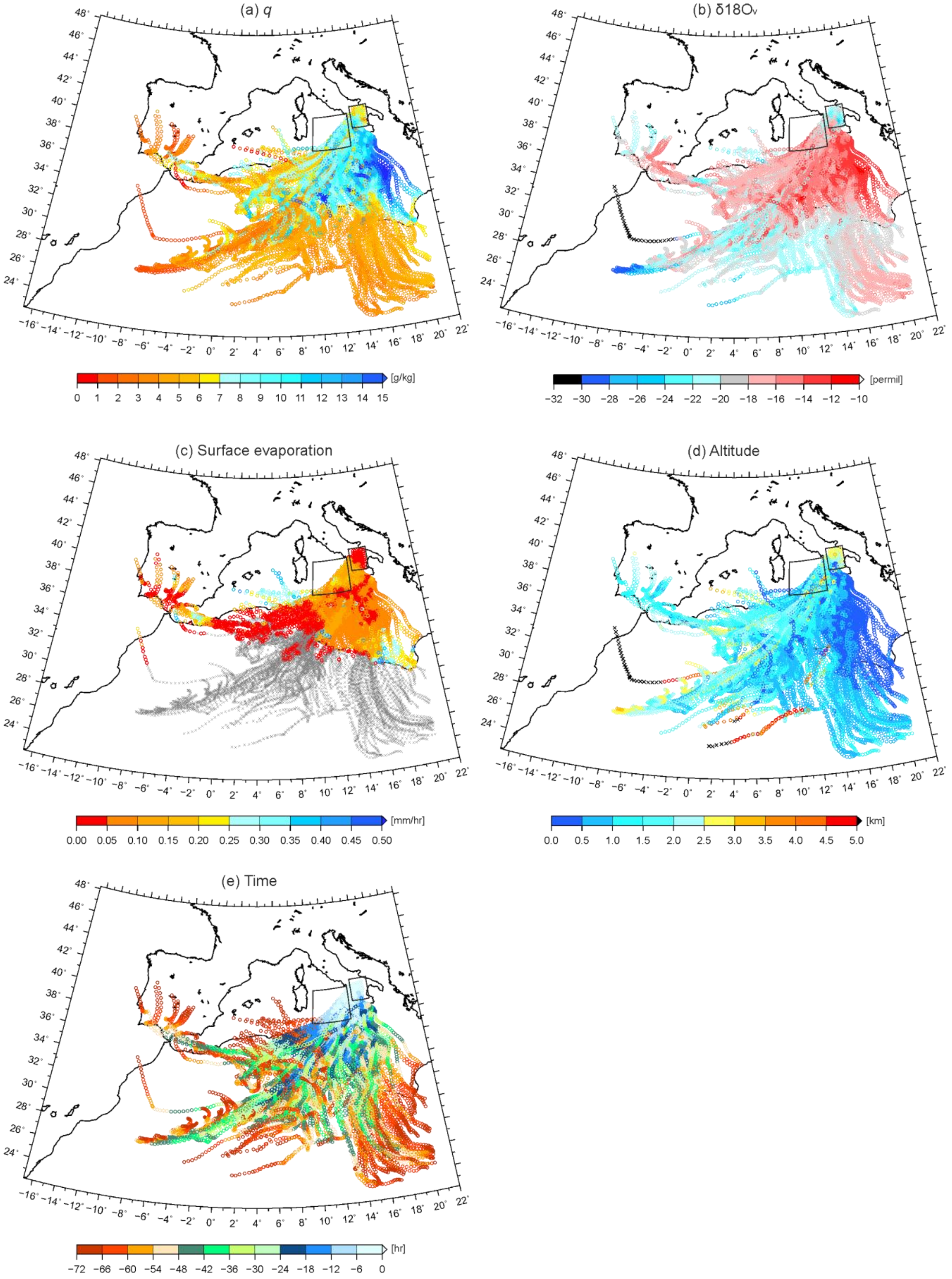

Figure 11. Same as Figure 7 but for the air parcel arriving at SI in layer of 800−700 hPa at 00 UTC on 16 October 2012.

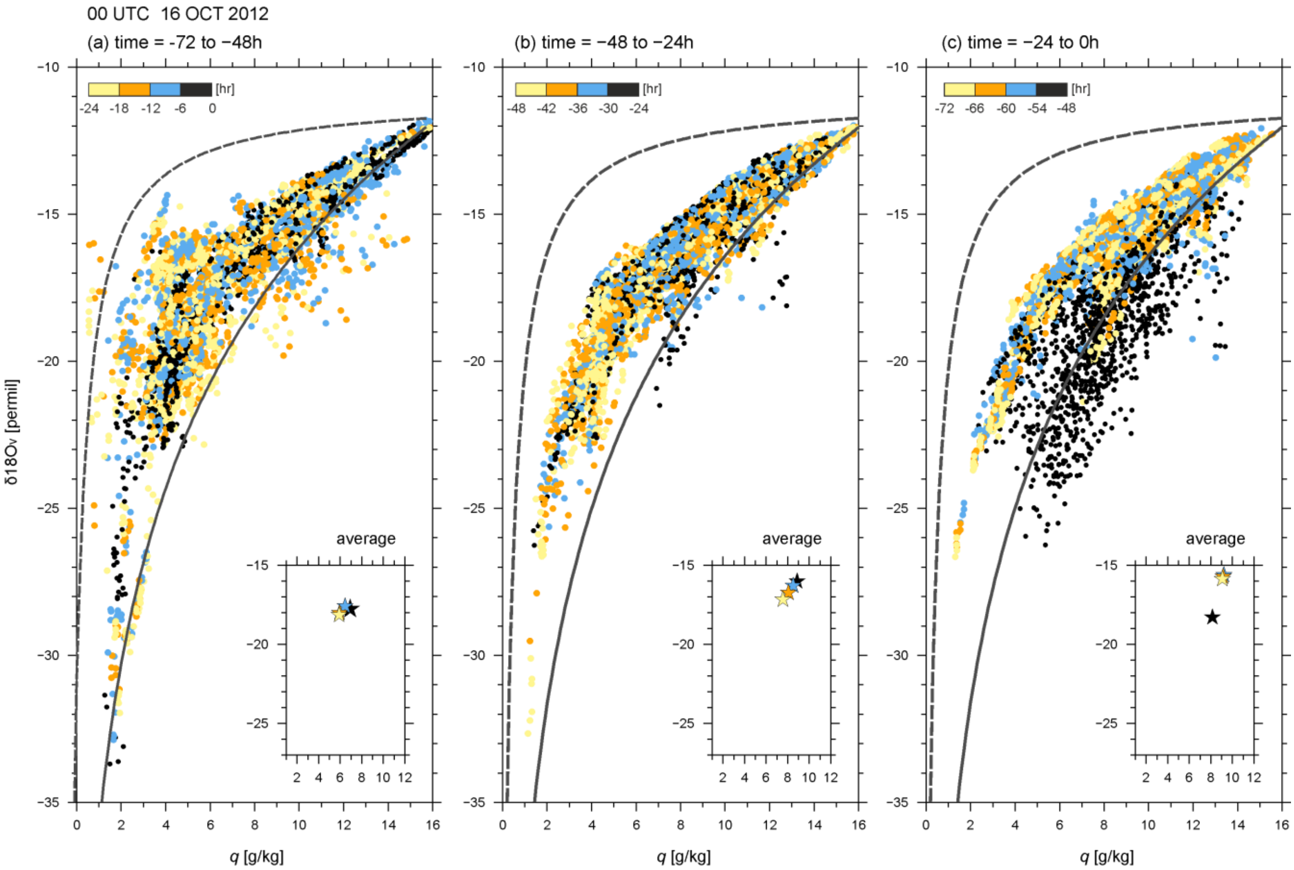

Figure 12. Scatter diagram of q and $\delta^{18}O_v$ along the backward trajectories of Figure 11 during (a) the times between −72 and −48 h, (b) times between −48 h and −24 h, and (c) times between −24 h and 0 h from 00 UTC on 16 October 2012 every 6 hours. The colour of dot changes every 6 h. The mixing and Rayleigh lines are indicated by dashed and solid line, respectively. The averaged q and $\delta^{18}O_v$ every 6 hours is displayed in the bottom right corner of each panel.

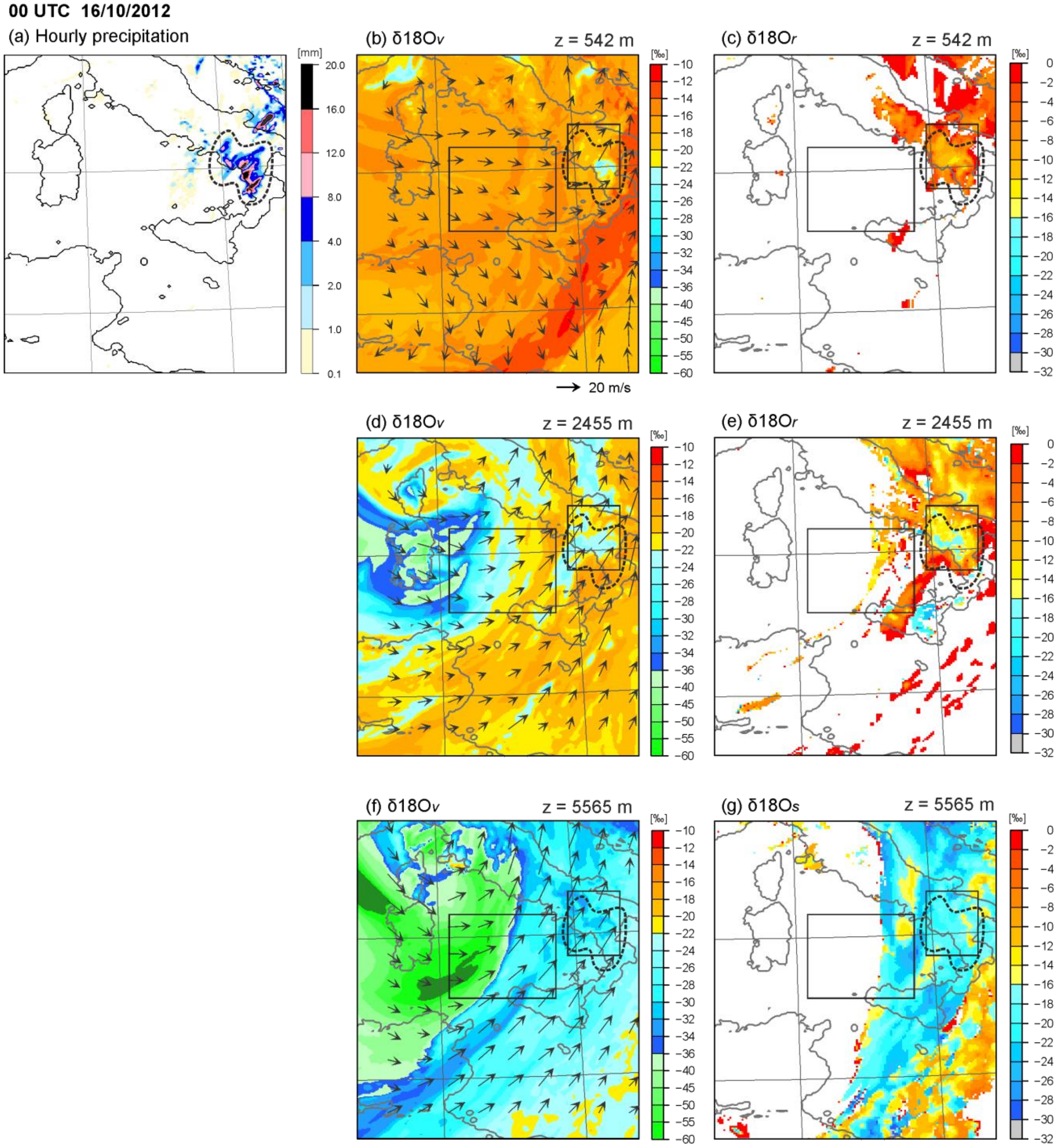

Figure 13. Same as Figure 10 but for 00 UTC on 16 October 2012.

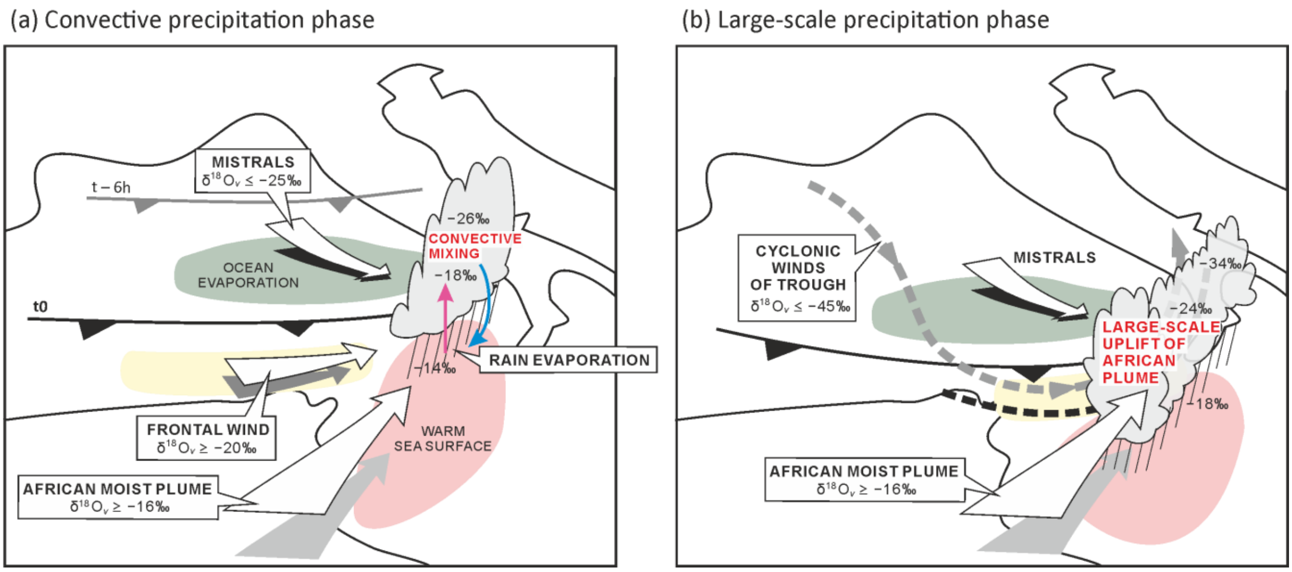
(a) Convective precipitation phase

(b) Large-scale precipitation phase

Figure 14. Schematics summarizing the main features of water vapour isotopologues and processes for deep convection upstream of SI and leading to the Phase 1 (a) and Phase 2 (b) of the HPE. In (a) and (b), white descending arrow indicate the mistral wind behind the edge of the cold front (thick black line). The white arrow in the yellow-shading encapsulated area illustrates the frontal wind at 850 hPa, and white arrow in the red-shading encapsulated area (warm sea surface) indicates the elevated African moist plume. In (a), convective ascent and precipitating downdraft is depicted by red and blue arrows, respectively. In (b), the southern edge of upper trough is indicated by black dashed line and the cyclonic flow of the trough is indicated by grey dashed line.